

Morphology of multilayer Ag/Ag(100) films versus deposition temperature: STM analysis and atomistic lattice-gas modeling

K. J. Caspersen,¹ C. R. Stoldt,^{1*} A. R. Layson,¹ M. C. Bartelt,² P. A. Thiel,¹ and J. W. Evans³

¹*Department of Chemistry and Ames Laboratory, Iowa State University, Ames, Iowa 50011*

²*Department of Chemistry and Materials Science, Lawrence Livermore National Laboratory, Livermore, California 94550*

³*Department of Mathematics and Ames Laboratory, Iowa State University, Ames, Iowa 50011*

(Received 22 September 2000; published 29 January 2001)

Scanning tunneling microscopy is used to analyze the nanoscale morphology of 25 ML films of Ag deposited on Ag(100) at temperatures (T) between 55 and 300 K. A transition from self-affine growth to “mound formation” occurs as T increases above about 140 K. The roughness decreases with increasing T up until 140 K in the self-affine growth regime, and then increases until about 210 K before decreasing again in the mounding regime. We analyze mounding behavior via a lattice-gas model incorporating: downward funneling of depositing atoms from step edges to lower fourfold hollow adsorption sites; terrace diffusion of adatoms with a barrier of 0.40 eV leading to irreversible island formation in each layer; efficient transport of adatoms along island edges to kink sites; and downward thermal transport of adatoms inhibited by a step-edge barrier of 0.06–0.07 eV along close-packed step edges (but with no barrier along kinked or open steps). This model reasonably recovers the T -dependence of not just the roughness, but also of the mound slopes and lateral dimensions above 190 K. To accurately describe lateral dimensions, an appropriate treatment of the intralayer merging of growing islands is shown to be critical. To describe behavior below 190 K, one must account for inhibited rounding of kinks by adatoms at island edges, as this controls island shapes, and thus the extent of open steps and of easy downward transport. Elsewhere, we describe the low- T regime of self-affine growth (with no terrace diffusion) accounting for a breakdown of the simple downward funneling picture.

DOI: 10.1103/PhysRevB.63.085401

PACS number(s): 68.55.-a, 68.37.Ef, 68.35.Fx

I. INTRODUCTION

The kinetic roughening of growing films has been a topic of intense interest in the statistical physics community since the mid-1980's.¹ The emphasis in such studies was primarily on long-time asymptotic properties for generic growth models, where often noise-induced roughening produced self-affine film morphologies. In 1991, Villain² recognized that a rather different growth mode occurs in the presence of an additional Ehrlich-Schwoebel step-edge barrier,³ which inhibits downward thermal transport of adatoms relative to intralayer transport. This barrier produces a growth instability resulting in the formation of “mounds,” a scenario which is common in homoepitaxial growth.⁴ However, the current understanding of such unstable growth processes is incomplete, and theoretical investigations continue with the goal of elucidating kinetic roughening in terms of mound coarsening and possible slope selection.^{4,5} Experimental studies have also become common, particularly in the 1990's, often comparing measured growth exponents with theoretical values predicted for various universality classes.^{1,4} In homoepitaxial growth, mound formation has been observed in several metal and semiconductor systems, and attempts made to extract exponents both for roughening and mound coarsening.⁴ Of particular relevance here are studies of metal(100) homoepitaxy, where kinetic roughening and mound formation has been observed for Cu,⁶ Fe,⁷ and Ag.^{8–10}

However, often for applications of thin films, it is not the asymptotic behavior of roughening which is relevant, but rather the morphology of films which have a thickness of a few layers to a few dozen layers. Desired magnetic proper-

ties, conductivity, catalytic activity, etc., often depend sensitively on film morphology, and, in particular, on roughness.¹¹ It is thus natural to explore how the morphology of such films depends on deposition conditions (substrate temperature, T , and deposition flux, F). In fact, a basic goal of nanotechnology, and a desired outcome of such studies, is the ability to “tune” nanoscale film morphology by suitable control of deposition conditions. There are surprisingly few studies which consider the temperature dependence of film growth (let alone provide a systematic analysis). Furthermore, such studies could be instructive for analysis of asymptotic roughening behavior. Most system specific modeling of roughening is based on (and potentially over interprets) limited data, typically for growth at a only single temperature,⁴ where one is often not even sure if asymptotic behavior has been achieved. Availability of data for a range of temperatures would help offset these problems.

Another basic goal is to develop atomistic models for growth which are sufficiently realistic to have quantitative predictive power. The development of such models also greatly promotes our understanding of the key atomistic processes controlling the morphology of the growing film. Some success has been obtained in modeling Fe/Fe(100) growth at room temperature,^{12,13} and also Pt/Pt(111) growth.¹⁴ However, the potential of such modeling to predict the T -dependence of growth has not yet been fully tested. Such a test is provided by the present comprehensive study of the T -dependence of Ag/Ag(100) film growth, which extends our previous more limited analysis.⁹

In Sec. II, we briefly review the details of the experimental component of our study, which utilizes variable-temperature scanning tunneling microscopy (VTSTM). A

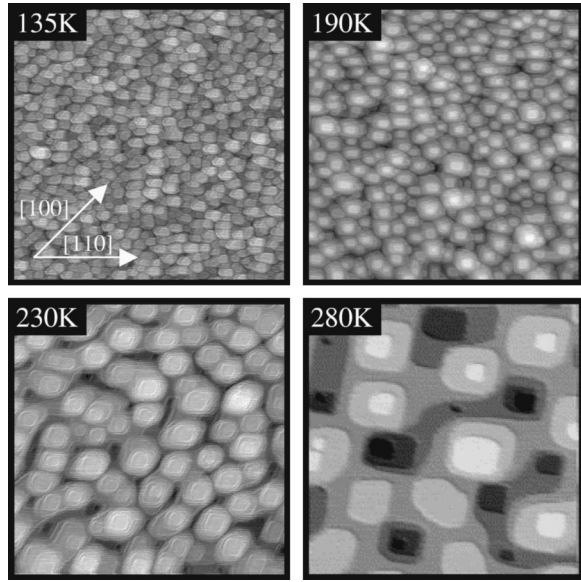


FIG. 1. Differentiated $100 \times 100 \text{ nm}^2$ STM images of 25 ML Ag/Ag(100) films deposited with $F \approx 0.02 \text{ ML/s}$ at various temperatures (shown). Darker (brighter) regions are lower (higher). Arrows indicating directions are labeled by the surfaces resulting from cleaving orthogonal to the arrows.

comprehensive analysis is presented in Sec. III of our experimental data for 25 ML Ag/Ag(100) films deposited at temperatures between 50 and 300 K. A general discussion of the atomistic mechanisms underlying the observed growth is presented in Sec. IV. Based on this discussion, detailed atomistic models are presented in Sec. V for growth above about 135 K, where mound formation is observed. The predictions of these models are presented in Sec. VI, and a detailed comparison is made with experiment. Our findings are summarized and future work discussed in Sec. VII.

II. EXPERIMENTAL DETAILS

Thin films of Ag were deposited on an Ag(100) single crystal surface held at temperatures (T) between 55 and 300 K with a flux of $F \approx 0.02 \text{ ML/s}$. The epitaxial adsorption sites on perfect terrace on this fcc(100) surface form a square array with a lattice constant of $a = 2.89 \text{ \AA}$. The crystal was mounted in an ultra-high vacuum (UHV) chamber with a base pressure below 1×10^{-10} Torr. The deposition source was an Omicron EFM3 UHV evaporator containing pure Ag. The morphology of the thin films was examined using an Omicron VTSTM. Liquid nitrogen was used for cooling of the substrate down to 135 K, while liquid helium was used to achieve lower T down to 55 K. The temperature during deposition and subsequent imaging remained fixed to within ± 5 K. The morphology of the deposited film was analyzed above the central portions of broad atomically flat terraces on the substrate. In this way, we minimize the influence of steps and other defects on the observed morphology of the deposited film. Images are taken as soon as possible after deposition (15–30 min.) to limit post-deposition restructuring or smoothing, but we believe that these effects are small (and, in fact, negligible below 260 K). Figure 1 shows typical

VTSTM images for films deposited at four different temperatures.

III. ANALYSIS OF STM DATA FOR 25 ML Ag/Ag(100) FILMS

A. Film height distribution

The key quantity characterizing vertical structure is the film height distribution. Clearly, the heights of atoms (and terraces) in growing homoepitaxial films take a periodic set of discrete values separated by the interlayer spacing, $b = a/\sqrt{2} = 2.04 \text{ \AA}$, for Ag(100). However, line scans from the VTSTM produces a quasi-continuous distribution, Φ_h , of heights, h . This distribution is normalized via $\int dh \Phi_h = 1$, and describes the fraction of the apparent surface (as probed by the STM tip) at a specific height, h . Also, the first moment $\int dh h \Phi_h = h_{av}$ gives the mean film height. In the distributions, Φ_h , regularly separated peaks are typically evident. The positions of the peaks correspond to the heights of atomic layers, so the separation between them must coincide with b (and, in fact, this observation is used to achieve precise calibration of the vertical scale in the STM line scans). The observed continuous height distribution reflects various features of the STM probe: the tip tracks the electronic (rather than physical) topography in a way that depends on tip shape; the response of the tip to height changes is not instantaneous; etc.

From Φ_h , it is natural to extract a discrete height distribution, Φ_j , which describes the fraction of surface atoms in discrete layer j ,¹⁵ and which is more appropriate for comparison with results from atomistic modeling. This was accomplished by deconvoluting Φ_h using a specified fitting function, G_h^j , for the contributions from layer j . Here, G_h^j has the properties $\int dh G_h^j = \Phi_j$, $\int dh h G_h^j / \int dh G_h^j = j b$, and $\Phi_h \approx \sum_j G_h^j$. It follows that $\sum_j \Phi_j = 1$ and $\sum_j j \Phi_j = j_{av}$, where $h_{av} \approx j_{av} b$. The most appropriate form for the G 's depends on the exact nature of the deviation of Φ_h from a discrete distribution, which involves nontrivial issues mentioned above, such as the tip shape, tip current, substrate morphology, etc. Thus, a simplification was made by choosing all G_h^j to be Gaussians. The deconvolution of Φ_h was performed via a linear least-squares fit of multiple Gaussians (one per peak), with the only constraint being that the Gaussian centers were equally separated. Figure 2 gives examples of Φ_h , and the corresponding G 's for two temperatures.

Next, we determine the key moments of the height distributions, Φ . Below, to facilitate comparison between continuous and discrete distributions, we always measure h in units of b . The most important quantity is the surface roughness, W (the root-mean-square width of the film height distribution), where $W_c^2 = \int dh (h - h_{av})^2 \Phi_h$ and $W_d^2 = \sum_j (j - j_{av})^2 \Phi_j$, for continuous (c) and discrete (d) distributions, respectively.¹ Figure 3 shows both these values of W for 25 ML Ag/Ag(100) films deposited over a temperature range from 54 to 300 K. Note that the former values are larger, except at higher T where terraces are so broad that Φ_h effectively reduces to a discrete distribution. The variation of W with T shows remarkable structure, for W increases from 300

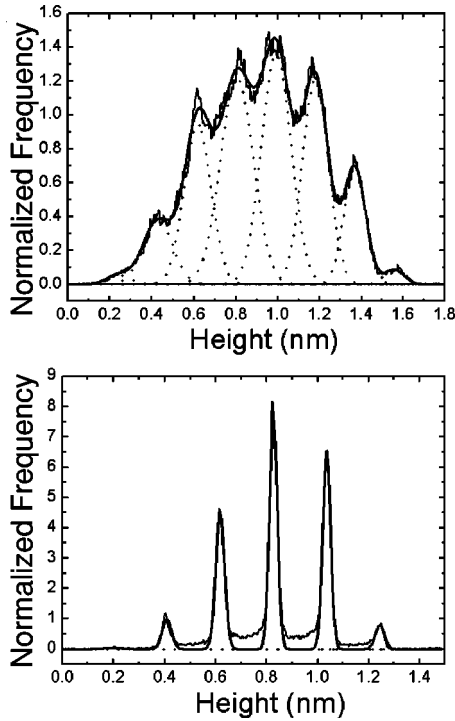


FIG. 2. Examples of the deconvolution of VTSTM height distributions of 25 ML Ag/Ag(100) films deposited at: (a) 230 K; and (b) 280 K. The thin solid line is the VTSTM distribution. The dotted lines are the individual Gaussian fitting functions, and the thick solid line is their sum.

to 205 K, then decreases from 205 to 135 K, and then increases again for temperatures lower than 135 K (at least to 55 K). We elucidate this behavior in later sections.

From the same experimental Φ , we also calculated the skewness of the film height distribution, $\kappa_c = W_c^{-3} \int dh (h - h_{av})^3 \Phi_h$ and $\kappa_d = W_d^{-3} \sum_j (j - j_{av})^3 \Phi_j$. These quantities give a measure of the lack of vertical reflection symmetry in the film surface. In addition, we determined the kurtosis of the height distribution, $Q_c = W_c^{-4} \int dh (h - h_{av})^4 \Phi_h - 3$, and

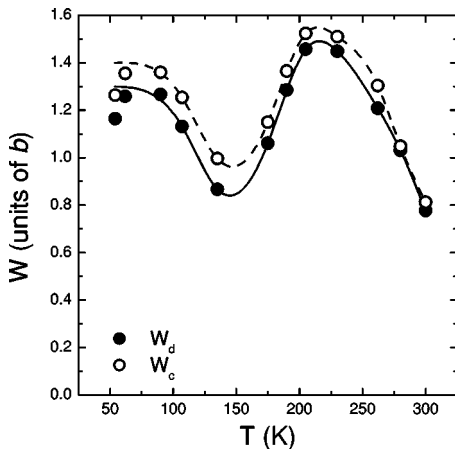


FIG. 3. W vs. T for 25 ML Ag/Ag(100) films deposited with $F \approx 0.02$ ML/s obtained from both the continuous (W_c) and discrete (W_d) film height distributions.

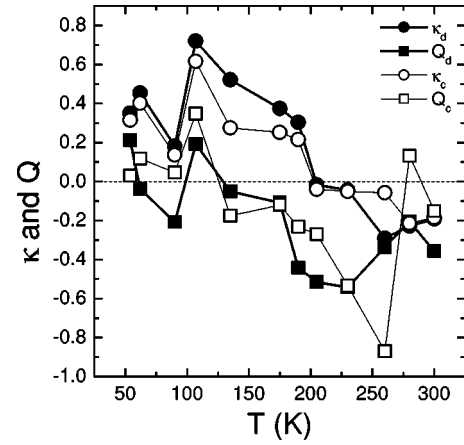


FIG. 4. κ and Q vs. T for 25 ML Ag/Ag(100) films deposited with $F \approx 0.02$ ML/s obtained from both the continuous (κ_c and Q_c) and discrete (κ_d and Q_d) film height distributions.

$Q_d = W^{-4} \sum_j (j - j_{av})^4 \Phi_j - 3$. This quantity, Q , measures the weight of the height distribution contained in the tail, relative to a Gaussian distribution (where $Q = 0$). Figure 4 shows the variation of both κ and Q with T . Despite the uncertainty in the data, there is a clear decrease from positive to negative values of κ with increasing T above about 110 K (and small systematic difference between κ_c and κ_d). The data for Q is noisier, but reveals systematically nonzero values.

B. Other aspects of the film morphology

For a more complete description of film morphology beyond its vertical structure (characterized by Φ and its moments), the lateral structure should also be quantified. For this purpose, we use primarily the height-height correlation function, $H(r)$. In a continuous representation of the height of the film surface, $H(r)$ gives the mean-square height difference for two points on the film surface separated laterally by a displacement, r . It follows that $H(r)$ vanishes for zero separation, and $H(r)$ can be shown to approach $2W^2$ for large separations.^{1,15} Also, $H(r)$ exhibits other general features depending on the nature of the film morphology:¹ (i) If the film surface has a fractal-like self-affine structure (characterized by a continuous spectrum of length scales), then $H(r)$ is monotonically increasing with $r = |r|$. It has the form $H(r) \sim r^{2\alpha}$ before reaching its saturation value of $2W^2$, where α is a roughness exponent. (ii) If the film surface is characterized by a somewhat ordered array of protrusions or “mounds” with a well-defined characteristic lateral size, then $H(r)$ displays damped oscillations towards its asymptotic value of $2W^2$. The value, R_{av} , of $r = |r|$ at the first maximum of $H(r)$ represents one measure of the average mound radius, while the value, D_{av} , at the first minimum represents a corresponding measure of the average mound diameter (so one expects that $D_{av} \approx 2R_{av}$).

Figure 5(a) shows typical $H(r)$ behavior (measured in the direction along close-packed [110] step edges) at various temperatures. The key feature is that strong oscillations in $H(r)$ occur for $T \geq 175$ K, but the oscillations are negligible or absent for $T \leq 135$ K. This suggests a transition from

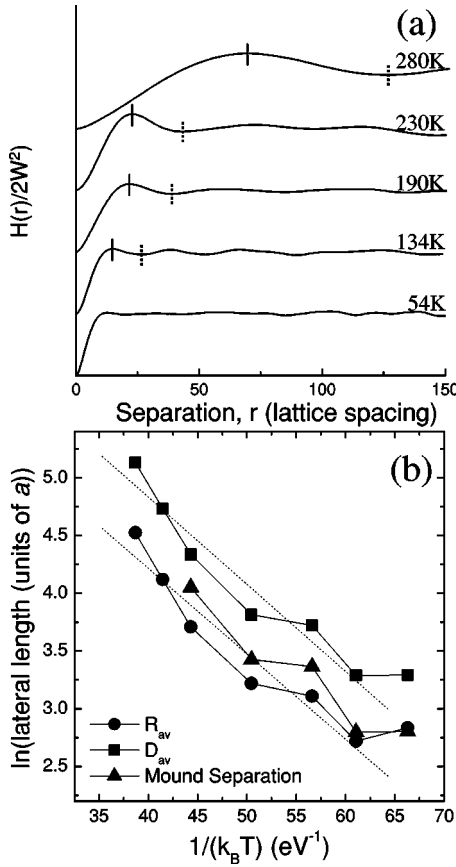


FIG. 5. (a) A family of $H(r)$ curves for various T , displaced vertically for clarity, and normalized by dividing by $2W^2$. Solid (dotted) vertical line segments indicate values of R_{av} (D_{av}). (b) Arrhenius plot of R_{av} (circles), D_{av} (squares), and the average mound separation (triangles) for $175 \text{ K} \leq T \leq 300 \text{ K}$ for 25 ML Ag/Ag(100) films deposited with $F \approx 0.02 \text{ ML/s}$. For D_{av} (R_{av}), the slope of the linear fit for $190 \text{ K} \leq T \leq 300 \text{ K}$ is -0.075 eV (-0.074 eV).

mounding to self-affine growth somewhere between 175 and 135 K. The existence of a transition is further supported by examination the T -dependence of the roughness exponent, α .¹ Rather than using $H(r)$, it is more convenient to estimate α from the (restricted) film roughness, $W_L \sim L^\alpha$, observed in a finite $L \times L$ “observation window” produced by STM line scans of length L .¹⁶ Figure 6 shows that for $T \geq 175 \text{ K}$, one has $\alpha \approx 1$, which is consistent with mounding morphologies, while for $T < 135 \text{ K}$, one has $\alpha \approx 0.5$, which is consistent with self-affine morphologies. Further indirect evidence for the existence of a transition in growth mode around 135 K comes from our analysis of the local surface slopes, described below.

In the mounding regime, the two quantities, D_{av} and R_{av} , decrease rapidly with decreasing temperature down to approximately 190 K, then remain virtually constant for lower temperatures. The relation $D_{av} \approx 2R_{av}$ is satisfied to within the experimental uncertainty. An Arrhenius analysis [Fig. 5(b)] of R_{av} and D_{av} for $T \geq 190 \text{ K}$ yields an energy of $E_c \approx 0.074 \text{ eV}$. Below, we argue that the physical significance of E_c is in its relationship to the terrace diffusion barrier, E_d [here for Ag on Ag(100)] via $E_d \approx 6E_c$.

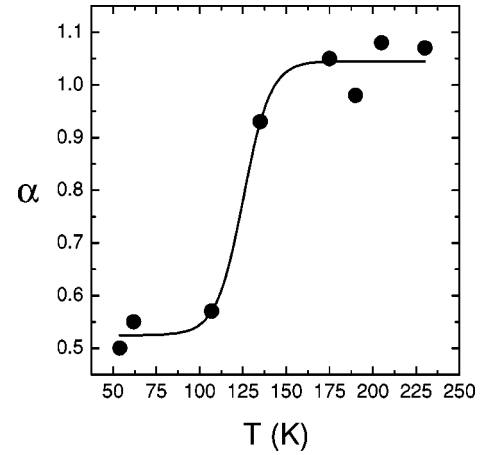


FIG. 6. α vs. T for 25 ML Ag/Ag(100) films deposited with $F \approx 0.02 \text{ ML/s}$. The curve is to guide the eye.

We also determined the typical surface slope using a variety of prescriptions. Of course, the slope provides a connection between the vertical roughness (W) and lateral characteristic lengths (R_{av} or D_{av}). In our analysis, we first determine the local slope, S , for each pixel in the VTSTM image by fitting a quadratic (second order) surface to its neighboring environment. From this local slope, S , two slope distributions were formed as shown in Fig. 7, one from the entire surface, and the other only from a restricted portion of the surface near mound sides. To characterize the latter, consider the “slope surface” obtained by plotting S as a function of lateral position. We identify the sides of mounds as locations where at least one of the two principal curvatures of this “slope surface” is negative.¹⁷

Upon examination, we find that the peaks of the distributions are slightly smaller than the averages. This is somewhat surprising since it was generally believed that the peak of these distributions would correspond to the slope of the mound sides,¹⁸ and the mound sides having the greatest slope would cause the peak to be greater than the average. However, we believe that the peak of the histograms partly reflects the substantial transition region between mound sides

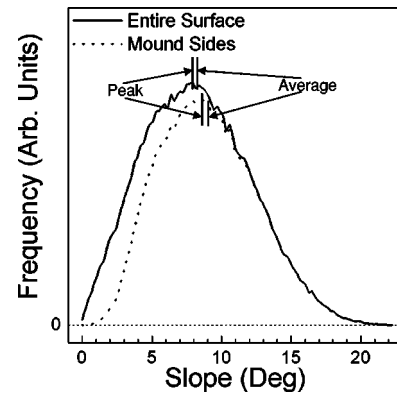


FIG. 7. Example of the distribution of local slopes for a 25 ML Ag/Ag(100) film deposited at 205 K with $F \approx 0.02 \text{ ML/s}$, for the entire surface and for the “mound sides” (see text).

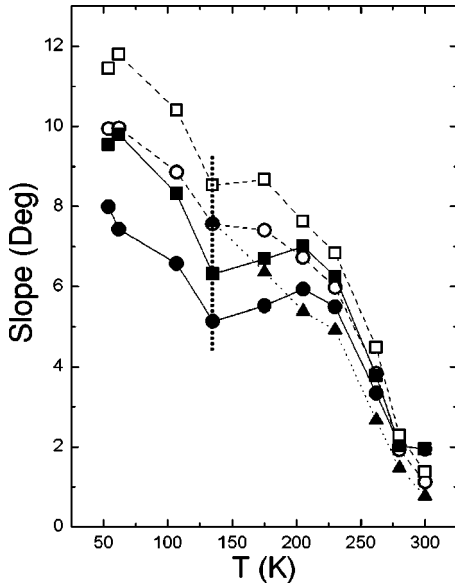


FIG. 8. Values for different prescriptions of local slopes vs. T for 25 ML Ag/Ag(100) films deposited with $F \approx 0.02$ ML/s. Circles correspond to sampling entire surface, whereas squares correspond to sampling mound sides. The solid lines with filled symbols represent the distribution peak, and the dashed lines with open symbols represent the average. Solid triangles show values obtained from the ratio W/R_c .

and tops, and between mound sides to the valley floor. These are the regions in greatest abundance in a “birds eye” view of the VTSTM images.

Figure 8 shows the variation with T various definitions of typical slopes (obtained from the peaks and averages of the full and restricted slope distributions). All of these increase as T is lowered from 300 K to roughly 200 K, and then remain virtually flat until 135 K, and finally increase again as T decreases below 135 K. This apparent nonanalytic slope discontinuity at 135 K provides further indication of the existence of a transition from mounding to self-affine growth at that temperature.

Also shown in Fig. 8 is another common measure of mound slope:¹⁹ the inverse tangent of W/R_c , where R_c is the lateral separation for which $H(r)$ first achieves $2W^2$. The traditional motivation for this selection was presumably that W provides an estimate of mound height, and R_c of mound radius. R_c is clearly smaller than our alternative estimate, R_{av} , of mound radius (but see below), however, it seems that W generally underestimates height, actually resulting in the ratio giving a smaller estimate of mound slope than produced by our direct estimates.

C. Tessellations for the mound distribution

In systems where mounds are well developed with fairly steep slopes,²⁰ their identity is unambiguous. However, this is not necessarily the cases for 25 ML Ag/Ag(100) films, especially for higher T . Thus, we developed a systematic definition or identification of mounds based on a prescribed decomposition or tessellation of the surface. This approach makes possible an unambiguous determination of the mound

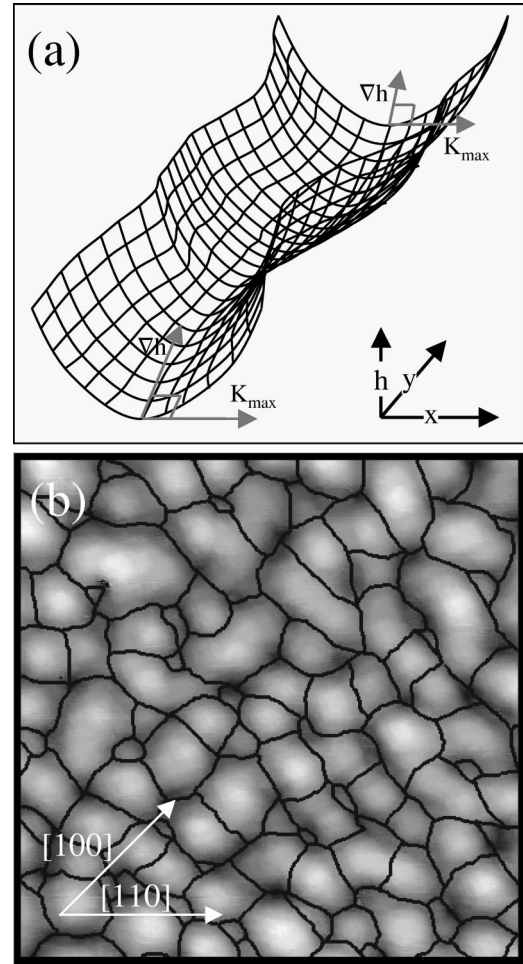


FIG. 9. (a) Schematic of our prescription for construction of tessellations of the film surface into mounds (where K_{\max} is the direction of maximum positive curvature). (b) A tessellation of an 80×80 nm² VTSTM image of a 25 ML Ag/Ag(100) film deposited at 230 K with $F \approx 0.02$ ML/s.

density, as well as a numerous other quantities characterizing mound structure. In this tessellation, boundaries between adjacent mounds are defined to be the bottom of the “valleys” on the film surface, or more exactly curves where the direction of maximum principal curvature, and the gradient vector, ∇h , for the film surface, are orthogonal [Fig. 9(a)]. Such curves can include the valleys of “flutes” on the sides of mounds (which terminate at points), as well as boundaries

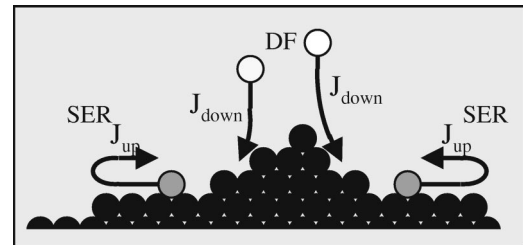


FIG. 10. Schematic of downward funneling (DF) and step-edge reflection (SER), as well as the associated induced lateral mass currents.

separating mounds. Any such terminating flute curves are removed from the tessellation. To determine these principle curvature and gradient vectors, we fit the film surface obtained from VTSTM images with the same fitting functions as used in the determination of the slopes. Small gaps or discontinuities in the resulting domain boundaries, caused by the imperfect fitting procedure and noise in the data, were then filled in by hand. Figure 9(b) shows these domain boundaries superimposed a VTSTM image of the surface of a 25 ML Ag/Ag(100) film deposited at 230 K. The above procedure is effective and can be applied for various T between 175 and 260 K, where mounds are visually evident. The mound density, N_m , was thus extracted, and the behavior of the corresponding measure of the mean mound separation, $L_m = (N_m)^{-1/2}$, is shown in Fig. 5(b) to be consistent with D_{av} and R_{av} . We emphasize that there is no simple precise relationship between these quantities. One might roughly equate L_m with D_{av} . However, making a new estimate of mound radius, R'_{av} , equating $\pi(R'_{av})^2$ to the mean area per mound, $(N_m)^{-1}$, yields $D'_{av} = 2R'_{av} = 2\pi^{-1/2}L_m \approx 1.13L_m$. From Fig. 5(b), one sees that D'_{av} seems to approach D_{av} only for higher T (but recall that the interpretation of D_{av} as the mean mound diameter is not precise either).

IV. DISCUSSION OF ATOMISTIC PROCESSES UNDERLYING GROWTH

Before presenting in detail the model that we employ to describe Ag/Ag(100) film growth, it is useful to discuss more generally the possible atomistic processes that could underlie our experimental observations. Over the experimental temperature range, the films grow with one of two distinct modes. As noted above, for “high” T above about 140 K, the film morphology is characterized by partially ordered array of protrusions or mounds (the “mounding regime”). Conversely, for “low” T below about 140 K, the morphology assumes a random fractal-like self-affine structure (the self-affine regime). In the Ag/Ag(100) system, it is known that the activation barrier for terrace diffusion is $E_d \approx 0.40$ eV with an attempt frequency of $\nu \approx 10^{13}$ /s.²¹ Thus, one can conclude that terrace diffusion is active in the mounding regime (at least above 150 K), but effectively inoperative in the self-affine regime.

First, we discuss the mounding regime. As a preliminary observation, we note that the presence of terrace diffusion leads to the diffusion-mediated nucleation and growth of two-dimensional islands in each layer. Furthermore, for the Ag/Ag(100) system, these processes are known to be effectively irreversible below about 320 K.²² From traditional nucleation theory, it is known that the mean island separation, L_{av} , scales like $L_{av} \approx 1.8(\nu/F)^{1/6} \exp[-E_d/(6k_B T)]$ (measured in units of surface lattice constant, a) for coverages around 0.1 ML.^{23,24} The scaling of the mean island density, $N_{av} = (L_{av})^{-2}$ automatically follows from this result.

With regard to mound formation, as noted in Sec. I, Villain² made the fundamental observation that this type of “unstable growth” is induced by the presence of an additional Ehrlich-Schwoebel barrier (E_{se}) at step edges which

inhibits downward transport (with total barrier $E_d + E_{se}$) relative to terrace diffusion (with barrier E_d).³ Such step-edge barriers can be due to the reduction of the coordination in the transition state for an atom hopping over an edge. These barriers cause some atoms to be reflected from descending steps, and produces biased incorporation at ascending steps. This “step edge reflection” (SER) produces a net lateral mass current, J_{up} , in the uphill direction, which, in turn, produces a growth instability (manifested by the formation of mounds). See Fig. 10. The step-edge barrier also enhances nucleation of islands in upper levels, and hence increases the population of atoms in higher levels. It should be noted that other mechanisms can produce a growth instability and mounding. These include attraction of diffusion atoms towards step edges,²⁵ and diffusion along step edges.²⁶ However, we have no evidence that these dominate the growth instability in the Ag/Ag(100) system, so we will attribute mounding primarily to the existence of a step-edge barrier.

Another key element of the film growth is the existence of downward funneling (DF) or deflection of atoms deposited at step edges (and perhaps at other microprotrusions) to lower four-fold hollow (4FH) adsorption sites corresponding to homoeopitaxy in fcc(100) systems.²⁷ It is clear that such DF produces a net lateral mass current, J_{down} , in the downhill direction, and, in fact, increases the population of lower levels in the growing film. In general, there is a delicate interplay between the effects of the step-edge barrier and DF during growth. For a perfect flat (singular) fcc(100) substrate, after some initial island formation, the uphill current, J_{up} , will typically dominate resulting in the development of mounds, such that the slopes of the mound sides increase with time or film thickness. However, as these slopes increase, so does the step density, and thus the amount of downward funneling and the magnitude of the downhill current, J_{down} . Eventually a slope is selected where the currents balance, i.e., $J_{up} + J_{down} \approx 0$.^{12,28} However, the film thickness required for slope selection, and the value of the selected slope, θ_s , depends on the deposition parameters. For higher T , where larger islands and lateral structures formed in the initial stages of growth, it would take longer to achieve slope selection if θ_s was independent of T . However, θ_s generally decreases with increasing T , partly countering this trend.

With the above background, the following overview of the growth process in the mounding regime can be developed. The relatively large smooth features that dominate the morphology at 300 K are the result of both the interlayer and intralayer diffusion processes being active. As the temperature is lowered to 200 K intralayer diffusion slows creating features with a smaller lateral length, also the E_{se} inhibits the interlayer diffusion process causing W to increase. For T below 200 K (down to 130 K) the inhibition of interlayer diffusion and the slowing of intralayer diffusion produce small features, such that the number of step edges becomes very large. Then the smoothing DF process dominates reducing W (down to 130 K). This nonmonotonic “re-entrant” smooth growth was first predicted in atomistic simulations for metal(100) homoeopitaxy.^{12,28}

Finally, we comment on the scaling of lateral mound sizes at least above 190 K. Since mounds are built upon a base of

a few submonolayer islands, one can imagine that the mean mound separation (and thus the diameter and radius) should scale like the mean submonolayer island separation, L_{av} . This explains our contention in Sec. II that $E_c \approx E_d/6$ (implying that $E_d \approx 0.44$ eV consistent with previous estimates²¹). The assumption in the above analysis is that the number of islands per mound is independent of T , a feature which is not clear given the varying influence of the step-edge barrier. However, analysis of our experimental and simulation data indicates that $D_{av}/L_{av} = 2.7, 2.9, 2.4$ for $T = 175, 225$, and 260 K, respectively, is roughly constant.

Second, we briefly discuss the self-affine regime, where an appropriate characterization of the deposition dynamics is key to understanding behavior. Even in the earliest molecular dynamics (MD) studies of deposition dynamics, it was recognized that atoms depositing on larger microprotrusions can get caught on the sides rather than funneling all the way down to lower 4FH sites.²⁹ While such larger microprotrusions have a negligible population at higher T , they become more prevalent at low T , so restrictions to downward funneling become an issue. For growth at extremely low T (near 0 K), no thermal diffusion processes are active, thus the film morphology is completely controlled by the deposition dynamics, which we describe as “restricted downward funneling” (RDF). The possibility for depositing atoms to get caught or trapped on the sides of microprotrusions in RDF leads to the formation of overhangs, and even internal voids or defects. This scenario was, in fact, observed in MD simulations of low T growth,³⁰ and its consequences discussed elsewhere.^{28,31,32} RDF also produces the growth of rougher films, consistent with the low- T data in Fig. 3.

Next, we consider behavior as T is increased above 0 K, but still in the regime where terrace diffusion is inoperative. Note that the trap sites for RDF are frequently of low coordination, and hence the activation barriers for interlayer diffusing out of these sites can be low. One example is for atoms trapped on the sides of $\{111\}$ microfacets, the activation barrier for diffusion is only 0.1 eV (in contrast to 0.4 eV for terrace diffusion). As a result, as T is raised above 0 K, these low barrier diffusion processes become increasingly active. Since most of the high coordination sites are in lower levels, the result is typically a net downward flow of atoms that works to make growth smoother. Thus, the drop in W from 50 to 140 K in Fig. 3 is attributed to these low barrier diffusion pathways becoming operative as T is increased. In fact, for large enough T (around 130 K), these diffusion pathways become so active that they essentially reproduce the DF behavior. Detailed modeling, described elsewhere,^{9,31,32} reveals that the density of internal voids vanishes just above 100 K. This is consistent with a claim by Miceli and co-workers³³ based on surface sensitive x-ray scattering data, that there exists a small population of internal defects in Ag/Ag(100) films grown at 100 K.

V. ATOMISTIC MODELS FOR MOUNDING IN AG/AG(100) FILM GROWTH

We have developed suitably tailored lattice-gas models which we believe effectively capture the essential atomistic

processes controlling Ag/Ag(100) film growth in the temperature range above about 135 K. These models are analyzed via kinetic Monte-Carlo (KMC) simulation. For such temperatures, we believe that these key processes are (cf. Sec. IV): terrace diffusion; irreversible island formation within each layer; rapid diffusion at island edges; inhibition of downward interlayer diffusion by the Ehrlich-Schwoebel step-edge barrier; and downward funneling of depositing atoms from step-edges and other micro-protrusions to lower 4FH sites.

In our models, we use the appropriate face-centered cubic crystalline geometry, selecting a (100) facet for the initial perfect substrate. Deposition occurs at randomly chosen locations at rate F (per site), and atoms follow DF deposition dynamics. Thus, atoms are allowed to occupy only 4FH sites, and as a consequence no overhangs or internal voids are formed. Isolated adatoms on flat terraces were then allowed to diffuse with a rate (per direction) given by the Arrhenius expression, $h = \nu_d \exp[-E_d/(k_B T)]$, with an activation barrier of $E_d = 0.40$ eV, and a prefactor of $\nu_d = 1 \times 10^{13} \text{ s}^{-1}$.²¹ Adatoms hop down a descending step-edge with rate reduced from h by a factor $\exp[-E_{se}/(k_B T)]$, where the additional barrier, E_{se} , can depend on the step structure, as described below.³⁴ (Thus, we assume a common prefactor, ν_d , for intra- and interlayer diffusion.) An isolated adatom diffuses until meeting another diffusing adatom, after which a new immobile island is irreversibly nucleated, or until irreversibly aggregating with a pre-existing island (either by intralayer terrace diffusion, or by downward diffusion at the island edge). In the case of aggregation, the final destination site for mobile adatoms at the island edge is determined by yet to be prescribed edge diffusion processes.

Semiempirical studies of energetics for diffusion processes,^{35,36} previous analysis of the sputtering of Ag(100),³⁷ and our own analysis of our own more extensive experimental data for Ag/Ag(100) film growth up to 100 ML,³⁸ suggest that the step-edge barrier, E_{se} , is negligible at kinked step edges (e.g., the open $[100]$ step edge) compared with straight closed-packed $[110]$ step edges. Thus, in our modeling, we assign a step-edge barrier $E_{[100]} = 0$ for adatoms descending at kink sites (where the transition state for hopping has roughly three supporting atoms), and a barrier of $E_{[110]} \geq 0$ for atoms descending at straight $[110]$ step edges (where the transition state for hopping has two supporting atoms). $E_{[110]}$ will be treated as a free parameter in fitting experimentally observed behavior. We also note that the process of descending from a step edge may actually involve exchange rather than simple hopping.^{35,36,39}

Finally, we describe in detail our treatment of edge diffusion. Below, we shall distinguish between “local corners” or single-atom high kinks (just referred to as kinks below) at the island edge, and “global corners” (which include the four extremities of the island, and also kinks with multiple height). An edge adatom will be able to round kinks (which is necessary to avoid a shape instability and the development of fractal islands^{40–42}), but not global corners (so isolated islands exhibit “rectangular fluctuations” from perfect squares, consistent with experiment). When a diffusing adatom aggregates with a pre-existing island, the adatom is

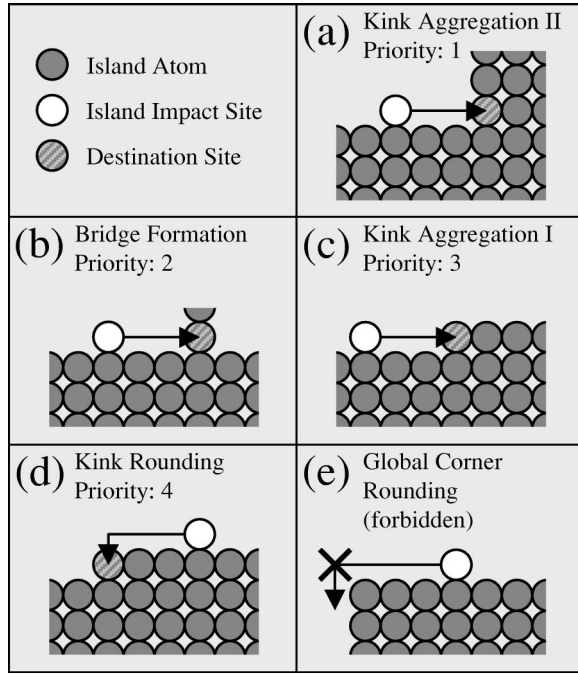


FIG. 11. Schematic of edge diffusion processes. Priority 1 is selected before priority 2, etc. (see text).

bound irreversibly to the island. However, its final destination is determined by accounting for the very rapid edge diffusion that occurs at these temperatures. (The barrier, E_{edge} , for diffusion along straight $[110]$ edges is only about 0.25 eV in this system.³⁹) Since the hop rate along these edges is so much larger than across terraces, we developed an algorithm that treats edge diffusion as instantaneous. After an adatom reaches the step edge, we check along the edge in *both* directions until a site with more than one occupied neighbor, or a corner site, is found. If one finds two global corners, as in Fig. 11(e), the atom remains where it impacted the island. Otherwise, the atom was placed in the multiply coordinated site with highest priority (see Fig. 11) that was found by the above procedure, rounding a kink site if necessary. We term this treatment of edge diffusion as the instantaneous kink rounding (IKR) model, since any kink rounding occurs instantaneously on the time scale of aggregation. See Fig. 12 for a schematic overview.

However, it is quite likely that there exists an additional “kink Ehrlich-Schwoebel” barrier, E_{kse} , to round kink sites [Fig. 11(d)], relative to the barrier E_{edge} to hop along straight $[110]$ edges. Then, the total activation barrier for kink rounding is $E_{\text{kr}} = E_{\text{edge}} + E_{\text{kse}}$. Studies using semiempirical potentials suggest barriers of $E_{\text{kse}} \approx 0.25\text{--}0.3$ eV to hop around corners.⁴³ Such barriers have also been used in the modeling of far-from-equilibrium step-edge nanostructures.⁴⁴ However, no definitive determination of E_{kse} exists. One should also consider the possibility of kink rounding by exchange,^{35,44} which one might expect is more likely than exchange at global corners, due to a more favorable transition state.⁴⁴ Below, we assign an attempt frequency of $\nu_e \approx 10^{12} \text{ s}^{-1}$ for edge diffusion processes.⁴⁴ Then, the key issue is whether kink rounding at rate⁴⁵ $h_{\text{kr}} = \nu_e \exp[-E_{\text{kr}}/(k_B T)]$ is

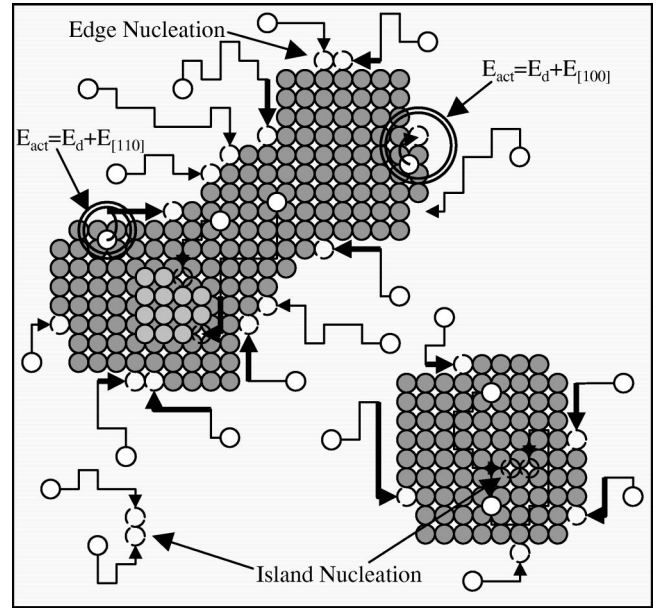


FIG. 12. Schematic of atomistic processes in the IKR model. The thicker lines and arrows represent the instantaneous edge diffusion in this model.

efficient on the time scale of aggregation of diffusion adatoms with each side of an island. The latter occurs at rate $h_{\text{agg}} \approx F/(4N_{\text{av}}) \sim 0.8 \nu_d (F/\nu_d)^{2/3} \exp[-E_d/(3k_B T)]$, using the scaling expression for N_{av} at coverages of around 0.1 ML.^{23,24} Here, we have assumed that the barrier E_{kr} limits kink rounding, rather than transport to the corner (the latter was assumed in Ref. 40). Then, corner rounding is efficient if

$$E_{\text{kr}} < (k_B T) [17.9 - (2/3) \ln F] + E_d/3.$$

Thus, for $F \approx 0.02$ ML/s, efficient kink rounding occurs only for $T > 200$ K if $E_{\text{kr}} \approx 0.49$ eV so $E_{\text{kse}} \approx 0.2$ eV, which is a plausible scenario based on analysis of experimental film morphologies (or for $T > 175$ K, if $E_{\text{kr}} \approx 0.44$ eV so $E_{\text{kse}} \approx 0.15$ eV). These low values for E_{kse} suggest that kink rounding may occur via exchange. Certainly, kink rounding is effectively inoperative in the lower T -regime of mound formation. With this in mind, we modified the IKR model to exclude all kink rounding, and describe this as the no kink rounding (NKR) model.

VI. MOUNDED FILM MORPHOLOGY PREDICTED BY ATOMISTIC MODELS

In the quantitative analysis of simulated film morphologies is presented in this Sec. VI, we set $E_d = 0.40$ eV, and treat the step-edge barrier $E_{[110]}$ as an adjustable parameter which is varied to match experimental observations. A common prefactor of $\nu_d = 10^{13} \text{ s}^{-1}$ is assumed for all thermal diffusion process. While the focus of this paper is on the morphology of 25 ML Ag/Ag(100) films, it should be noted that considerable insight into the atomistic processes and energetics controlling interlayer transport can be obtained from analysis of initial stages of growth. In Appendix A, we compare model predictions with the observed morphology of 1

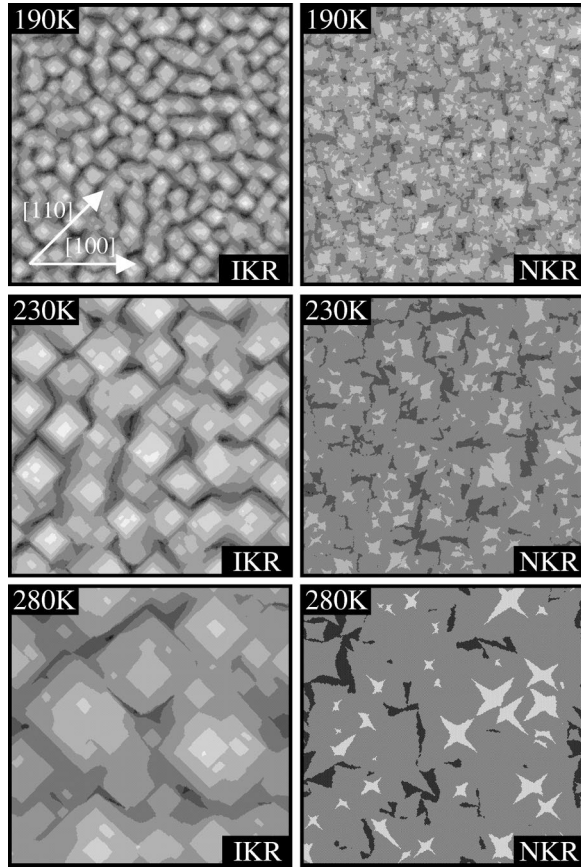


FIG. 13. $100 \times 100 \text{ nm}^2$ images for the morphologies of 25 ML Ag/Ag(100) films deposited with $F = 0.02 \text{ ML/s}$ at various temperatures (shown), as predicted by the IKR model and the NKR model.

ML films. Estimates of the step-edge barrier, $E_{[110]}$, can be compared with those obtained below from analysis of 25 ML films.

In Fig. 13, we show the morphologies of 25 ML films predicted from both the IKR and the NKR models for three different temperatures. As expected, the IKR model appears to match well the experimental morphologies shown in Fig. 1 at the higher $T = 230$ and 280 K , and even does reasonably well at 190 K . The 190 K morphology from the NKR model is also consistent with the experimental observations (especially given the possibility of some post-deposition restructuring of the lateral morphology may have occurred before STM imaging). However, NKR model morphologies at higher T do not match experiment, and display a shape instability in two-dimensional island growth deriving from the lack of corner rounding.^{40,41} Since the IKR model describes Ag/Ag(100) film growth for most of the T -range of interest, we also present a direct comparison of experimental and simulated film morphologies at 230 K (using a three-dimensional representation) in Fig. 14.

A. Film height distribution

In this subsection, we focus on the behavior of W_d , κ_d , and Q_d , which are determined from the film height distribution, $\Phi_j = \theta_j - \theta_{j-1}$, where θ_j is the coverage of layer j .

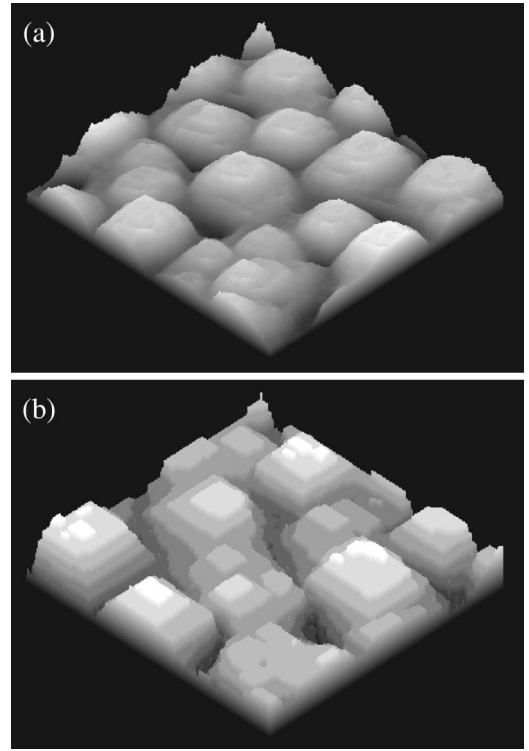


FIG. 14. $50 \times 50 \text{ nm}^2$ images of 25 ML Ag/Ag(100) films deposited at 230 K with $F = 0.032 \text{ ML/s}$: (a) experimental STM image; (b) simulation image from the IKR model. Note that STM imaging typically produces some “artificial” smoothing of features.

(Note that our simulations do not produce continuous versions of these quantities.) W_d from experiment and for both IKR and NKR models with various $E_{[110]}$ is shown in Fig. 15. For higher T above 200 K , the IKR model with $E_{[110]} = 0.06\text{--}0.07 \text{ eV}$ best matches experimental behavior. The match is poor for the IKR model below 200 K . This feature should be expected, since kink rounding is in fact strongly

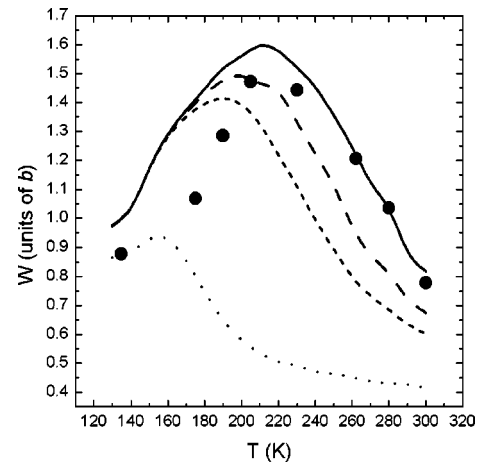


FIG. 15. W_d vs. T for 25 ML Ag/Ag(100) films deposited with $F \approx 0.02 \text{ ML/s}$ for experiment (solid circles), the IKR model with $E_{[110]} = 0.07, 0.06, 0.05 \text{ eV}$ (solid curve, long dashed curve, short dashed curve), and the NKR model with $E_{[110]} = 0.06 \text{ eV}$ (dotted curve).

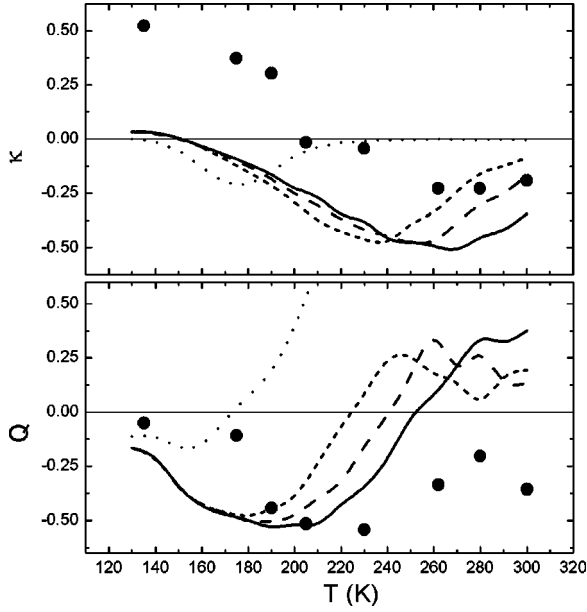


FIG. 16. κ and Q vs. T for 25 ML Ag/Ag(100) films deposited with $F \approx 0.02$ ML/s for experiment (solid circles), the IKR model with $E_{[110]} = 0.07, 0.06, 0.05$ eV (solid curve, long dashed curve, short dashed curve), and the NKR model with $E_{[110]} = 0.06$ eV (dotted curve).

inhibited in this regime. Overactive kink rounding in the IKR model produces islands that are too compact with an over abundance of the close packed $[110]$ step edges. Actual island morphologies should be more irregular than predicted by the IKR model, with more kinked step edges, making downward interlayer transport more efficient. To check this contention, we note that the NKR model does a good job of predicting the observed roughness for lower T around 140 K–160 K. However, the NKR model values for W_d deviate significantly from experiment for all higher T . Here, the complete inactivity of kink rounding in the NKR model produces artificially ramified star-like island shapes (Fig. 11), with an over abundance of kinked step edges and artificially active downward transport. In summary, for the IKR model, the over abundance of $[110]$ step edges with their large E_{se} produces W_d values that were too high at lower T . In the NKR model, the over abundance of kinked step-edges and their small E_{se} produces W_d values that are too small at higher T . Preliminary analysis shows that a model with finite E_{kse} can universally describe observed W_d behavior. Details will be presented elsewhere.

The simulation results for the higher moments, κ_d and Q_d , are compared with experiment in Fig. 16. Both quantities show significant deviations from experimental values, which we believe can be rationalized as follows. Due to its finite size, the STM tip has difficulty probing the bottoms of valleys of the film surface, this limitation becoming more severe for lower T where characteristic lateral lengths are smaller, and local slopes are greater. This effect produces a height distribution in which the probabilities of the lowest layers are artificially small. These differences are small enough for W_d to be virtually unaffected. However, κ_d and Q_d , being higher moments, are more sensitive to the shape

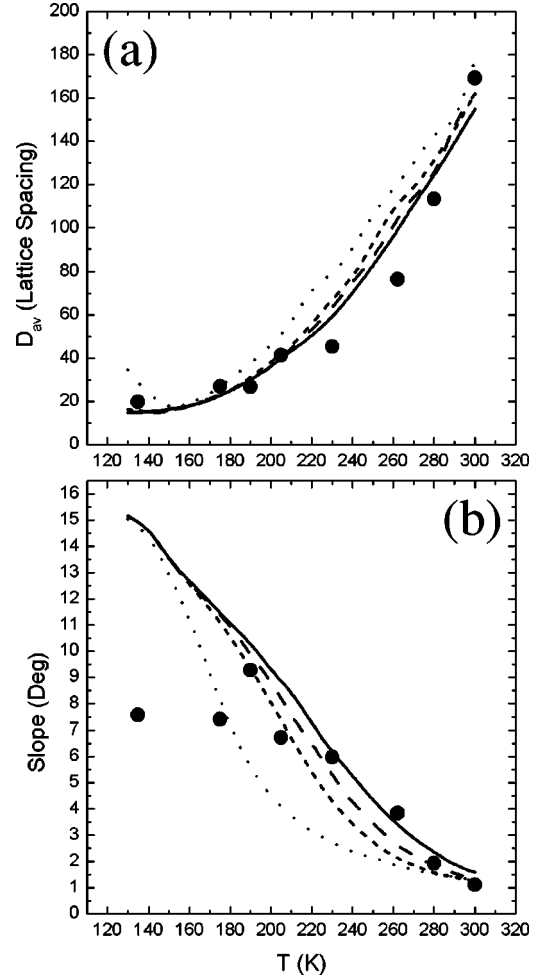


FIG. 17. (a) D_{av} and (b) local slope vs. T for 25 ML Ag/Ag(100) films deposited with $F \approx 0.02$ ML/s for experiment (solid circles), the IKR model with $E_{[110]} = 0.07, 0.06, 0.05$ eV (solid curve, long dashed curve, short dashed curve), and the NKR model with $E_{[110]} = 0.06$ eV (dotted curve). The local slope is an average over the entire surface for experimental data, and is obtained from the step density in the simulations.

of the height distribution, and are more greatly affected (particularly the odd moment κ). The simulated κ_d is more positive, and Q_d is more negative than in experiment. Thus, in comparing simulation with experiment, we focus more on comparing trends than matching the quantitative values for each T . Figure 16 shows that the IKR model, with $E_{[110]}$ as chosen above, does a reasonable job in this respect, and thus we believe that it accurately describes the basic features of the height distribution, especially for higher T .

B. Other aspects of the film morphology

Analogous to Sec. IV B, for a complete analysis of simulated morphologies (and for comparison with experiment), we examine the lateral morphology as characterized by the height-height correlation function, as well as the slope of the film surface. For comparison of lateral lengths, we will focus on only D_{av} . As seen in Fig. 17(a), D_{av} for the IKR model, and even the NKR model, compare favorably with experi-

ment for a range of values of $E_{[110]}$. This should not be surprising, for the major determining factor for the lateral length of the system is simply the terrace diffusion rate, which is controlled by the same E_d for all models. We emphasize that the mean mound separation, L_m , and diameter, D_{av} , are substantially larger than the mean island separation, L_{av} , in the submonolayer regime (see below). The E_d -value used in our simulations ensures the match to L_{av} . However, there is no *a priori* guarantee that the simulations will match D_{av} for 25 ML films. Indeed, experimental values of D_{av} are *not* matched if we use our previous simpler “square island” model for metal(100) homoepitaxial growth,^{9,12,24,28} where square islands within each layer that meet during growth do not restructure, but continue to grow as overlapping squares (see Appendix B). Thus, it is clear that a realistic treatment of the restructuring or merging of islands in the same layer is critical for describing the increase in lateral correlation length which is associated with mound formation during growth (at least in the case of systems with “small” step-edge barriers).

Next, in Fig. 17(b), we compare simulated local slopes with experimental values. The simulated slope was obtained by determining the density of step edges (in the direction aligned with $[110]$ step edges), weighting by step height. This corresponds roughly to the experimental local slope averaged over the whole surface, which is also shown in this figure. We see that for $T > 200$ K the experimental and simulation slopes match acceptably, however the simulated slopes are too large for lower T . In the IKR model, this is partly a consequence of the overestimation of W_d . We also expect that the step density may not correspond to the experimental measure of slope at low T , particularly in the NKR model, which has a large step density due to very irregular island shapes. Note that our modeling does not produce the slope discontinuity around 135 K observed in other experimental data. This may be because our models do not incorporate the breakdown in DF necessary to realistically describe the transition to low- T self-affine growth.^{31,32}

For comparison with the tessellated mound distribution obtained in the experimental STM image for a 25 ML Ag/Ag(100) film grown at 230 K (Fig. 9), we also show the corresponding tessellation for a simulated film morphology using the IKR model in Fig. 18. The procedure used here is identical to that applied in Fig. 9. Qualitative comparison of Figs. 9 and 18 indicates that the IKR model does reproduce the key features of the mound distribution. A comprehensive quantitative analysis of various features of the tessellated mound distribution will be presented elsewhere, but detailed comparison with experiment is inhibited by limited statistics for the latter.

C. Effect of downward funneling

As a definitive test of the notion that DF is responsible for the drop in W as T decreases from 200 to 130 K, we implemented the IKR model, and the NKR model, for a simple cubic (SC) crystalline geometry [where the initial substrate is a (100) facet]. In our implementation in a SC geometry, DF is completely absent, as all deposited atoms adsorb where

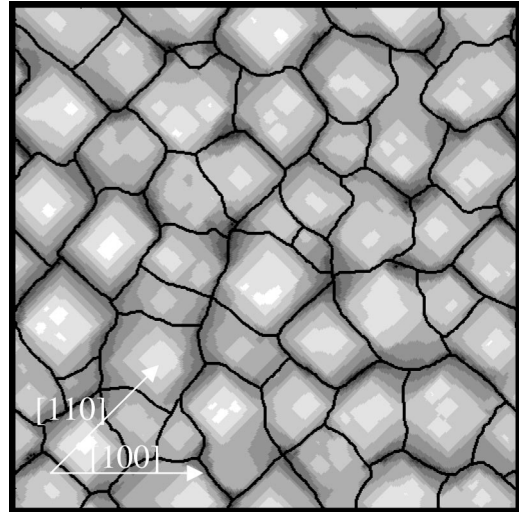


FIG. 18. Tessellation of an 80×80 nm² image generated from the IKR model of a 25 ML Ag/Ag(100) film deposited at 230 K with $F \approx 0.02$ ML/s.

they impinge at on-top sites directly above film atoms. Figure 19 shows the results for W_d for the SC models over the same temperature range as the FCC model results in Fig. 15. We see that W_d in the SC models do *not* show the same drop below 200 K as in the FCC models. Also, W_d for the SC models are larger for all T 's (substantially so for lower T). This should be expected since DF is a smoothing effect, which is amplified for lower T . Also, SC models should produce Poisson growth as $T \rightarrow 0$, for which $W_d = \theta^{1/2}$ (so $W_d = 5$ for 25 ML films).

That DF controls the drop in W is not unambiguous from the outset. One alternative is that the development below 200 K of irregular structures with a high population of kinked step edges (as a result from limited kink rounding) would also naturally enhance downward transport due to the zero step-edge barrier for kinked (versus $[110]$) step edges. In the SC NKR model, W_d is indeed much lower than in the IKR model for a range of T below 200 K, so it is possible that W_d

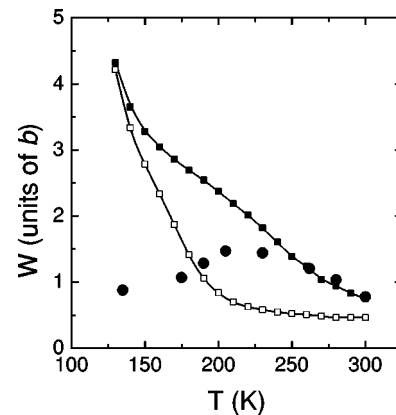


FIG. 19. W_d vs. T for 25 ML Ag/Ag(100) films deposited with $F \approx 0.02$ ML/s. Solid circles represent experimental data, while solid (open) squares correspond the SC version of the IKR (NKR) model.

could drop somewhat below 200 K in a model with a finite corner rounding rate. However, W_d would certainly achieve the same high value as in both the IKR and NKR models for lower T around 135 K. Consequently, such a model could not explain experimental observations.

Finally, we note another recently proposed idea⁴ that the “re-entrant” decrease in W with decreasing T is simply due to the higher density, and thus decreasing size, of islands (with decreasing T). More specifically, presumably the idea is that it is easier for atoms deposited on top of small islands to reach the edge and hop down. However, if valid, the decrease in W should appear in the SC models discussed above (and in the SC model described in Appendix B). This is not the case. The reason for the failure of this idea is simply that as T decreases and the islands become smaller, so does the terrace diffusion rate. Thus, it is not necessarily easier for adatoms to reach island edges. Furthermore, one should note that in any SC model, as T decreases and all thermal diffusion processes switch off, very rough Poisson growth must be achieved.⁹

VII. SUMMARY

In summary, our analysis of VTSTM data for deposited Ag/Ag(100) films provides the most comprehensive analysis to date of the T -dependence of the morphology of deposited metal(100) homoepitaxial films. We note that our results for the T -dependence of Ag/Ag(100) film growth are consistent with recent VTSTM studies of growth between 135 and 300 K by the Genova group¹⁰ (who also studied sputtering⁴⁶), and with the earlier observation based on surface-sensitive x-ray scattering of rougher growth at 200 than at 300 K.⁸ In our analysis, we have considered in detail both vertical and lateral aspects of the morphology, focusing on the regime of mound formation. Our lattice-gas modeling provides insight into the key atomistic processes and energetics controlling growth. For example, we find that a step-edge barrier of $E_{[110]} = 0.06\text{--}0.07$ eV along close-packed [110] step edges (compared with $E_{[100]} \approx 0$ eV along kinked or open step edges) is responsible for the mound formation. (This value for $E_{[110]}$ assumes a common prefactor for intra- and interlayer diffusion.) Downward funneling deposition dynamics is shown to be responsible for the re-entrant smooth growth below 200 K (at least down to 135 K). Also, the post-collision restructuring of growing islands within the same layer is shown to be a key ingredient in the development of mounds and the determination of their lateral dimension.

It should be emphasized that while our atomistic modeling has been quite successful, the IKR and NKR models that we have implemented are still rather idealized, being tailored to incorporate just the essential physics. We have already suggested the need to incorporate a finite kink Ehrlich-Schwoebel barrier, E_{kse} [rather than the extremes of $E_{\text{kse}} = 0$ for IKR, and $E_{\text{kse}} = \infty$ for NKR], in order to describe film morphology over the entire T -range from 135 to 300 K. We have also noted that our estimates for the step-edge barrier, $E_{[110]}$, correspond to assuming a common prefactor of $\nu_d = 10^{13} \text{ s}^{-1}$ for intra- and interlayer diffusion. Of course, there will be some difference between the prefactors,^{36,47} which

would modify the estimate of $E_{[110]}$. One could reduce the prefactor for interlayer diffusion (relative to that for terrace diffusion), and increase $E_{[110]}$, so the interlayer diffusion rate is unchanged at 230 K, say. Relative to the original model, this would inhibit (enhance) interlayer diffusion, and thus lead to an increase (slight decrease) in W above (below) 230 K. However, it is not clear that the fit to experimental data would be much improved, and similar refinements could perhaps be achieved by instead incorporating further variations in step-edge barrier. Another change might include nucleation or aggregation once a diffusing adatom reaches a site diagonally adjacent to (rather than directly adjacent to) another atom or island, a feature reflecting the low barrier to move from the diagonal to the directly adjacent site.⁴³ These modifications will be considered in future work.

In this paper, we have not discussed the dynamics of kinetic roughening or of mound coarsening (or given values for the associated exponents) for film growth at a fixed temperature. In more extensive experimental studies of Ag/Ag(100) film deposition up to at least 100 ML,³⁸ we find a strong T -dependence of these aspects of film growth, with slow selection of mound slopes for higher T ,⁹ and more rapid selection at lower T . Details will be reported elsewhere.

ACKNOWLEDGMENTS

K.J.C., C.R.S., A.R.L., P.A.T., and J.W.E. were supported for this work by NSF Grant No. CHE-0078596. Work was performed at Ames Laboratory, which is operated for the U.S. Department of Energy (U.S. DOE) by Iowa State University under Contract No. W-7405-Eng-82. M.C.B. was supported by the U.S. DOE. Lawrence Livermore National Laboratory is operated for the U.S. DOE by the University of California, under Contract No. W-7405-ENG-48.

APPENDIX A: INITIAL STAGES OF MULTILAYER GROWTH

We have used the IKR model with $E_d = 0.40$ eV, $E_{[110]} = 0.07$ eV, and $\nu_d = 10^{13} \text{ s}^{-1}$ (and $E_{[100]} = 0$ eV) to examine the initial stages of growth up to 1 ML at room temperature (300 K). We set $F \approx 0.055$ ML/s to match earlier experiments.²² In Fig. 20, we show simulated configurations at this T and F for coverages of 0.25, 0.5, 0.75, and 1.0 ML. Note that before island coalescence is significant, almost all step edges have the close packed [110] orientation. However, as a result of coalescence, a high population of kinked step edges are generated. Since these step edges have no step-edge barrier, their formation is significant in inhibiting the nucleation and growth of 2nd layer islands. Figure 21 shows the 2nd layer population at 1 ML versus $E_{[110]}$.

A single experimental study imaging a 100 nm \times 100 nm region revealed a 2nd layer coverage of $\theta_2 \approx 0.057$ ML.²² Then, from Fig. 21, we would estimate that $E_{[110]} \approx 0.09$ eV. However, it should be recognized that there is substantial uncertainty in the estimate of θ_2 from a single 100 nm \times 100 nm image. Simulations for this size region (with $E_{[110]} = 0.07$ eV) find a distribution of θ_2 values with a standard deviation of 0.0054 ML. Thus, the true (av-

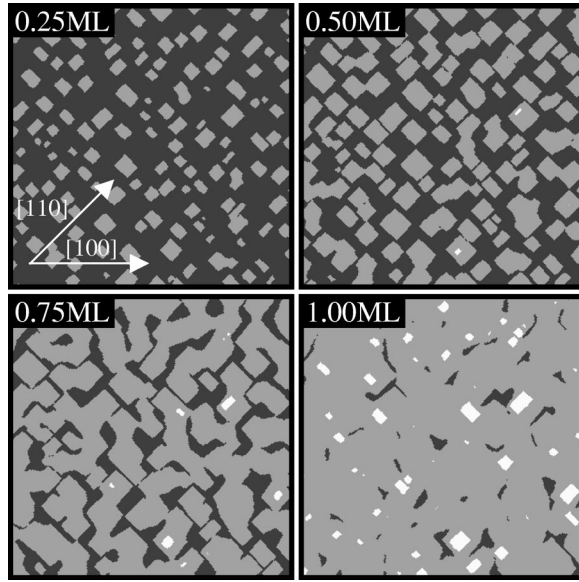


FIG. 20. $102 \times 102 \text{ nm}^2$ image of simulated film morphologies for initial stages of Ag/Ag(100) growth at 300 K with $F = 0.055 \text{ ML/s}$ from the IKR model with $E_{[110]} = 0.07 \text{ eV}$.

erage) experimental θ_2 could be as low as 0.050 ML, roughly consistent with a lower estimate of $E_{[110]}$ given in the text.

APPENDIX B: COMPARISON WITH “SQUARE ISLAND” GROWTH MODEL

In previous modeling of metal(100) homoepitaxy in this (Ag) and other systems, we focused on analysis of film roughness using a simpler canonical “square island” model.^{9,12,22,24,28} This model enforced square shapes for individual (isolated) islands in each layer, as well as specifying that when growing islands meet, they continued to grow as

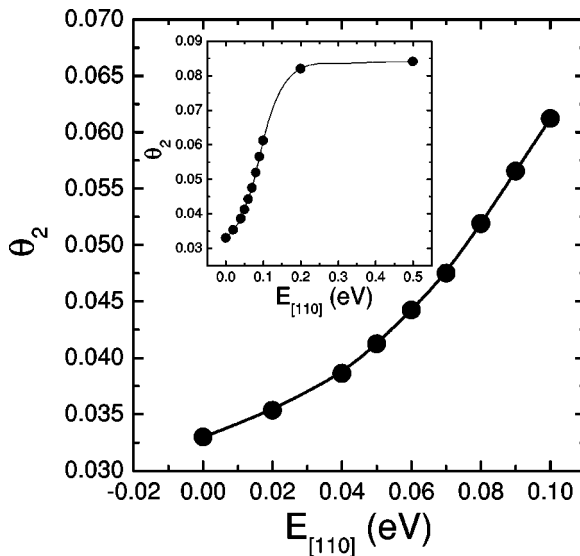


FIG. 21. Second layer coverage, θ_2 , vs. $E_{[110]}$ in the IKR model for 1 ML Ag/Ag(100) films deposited at 300 K with $F = 0.055 \text{ ML/s}$.

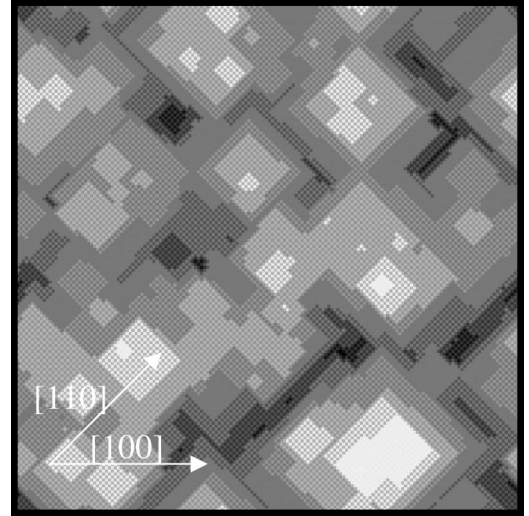


FIG. 22. $35 \times 35 \text{ nm}^2$ image of the “square island” model prediction for the morphology of a 25 ML Ag/Ag(100) film deposited at 230 K with $F \approx 0.02 \text{ ML/s}$.

overlapping square. Thus, there was no restructuring, or formation of dumbbell shapes seen in our more realistic IKR model (cf. Fig. 20). Consequently, in this “square island” model, only [110] step edges are present, so consistently we assume a uniform step-edge barrier. Otherwise, all the ingredients of the models described in the text [terrace diffusion leading to irreversible nucleation and growth of islands; downward funneling deposition dynamics for a fcc(100) crystal geometry] are incorporated.

Figure 22 shows the predictions of the “square island” model with an fcc(100) crystal geometry for W_d versus T for 25 ML films deposited with $F = 0.02 \text{ ML/s}$ with $E_d = 0.040 \text{ eV}$ and $\nu_d = 10^{13}/\text{s}$. Also the uniform barrier $E_{sc} = 30 \text{ meV}$ was chosen to best match the experimental data for Ag/Ag(100). As noted in previous studies,^{9,22} this barrier should be regarded as an effective value. Indeed, our more sophisticated modeling in Sec. VI shows that it corresponds to some sort of average of the values for kinked (or open),

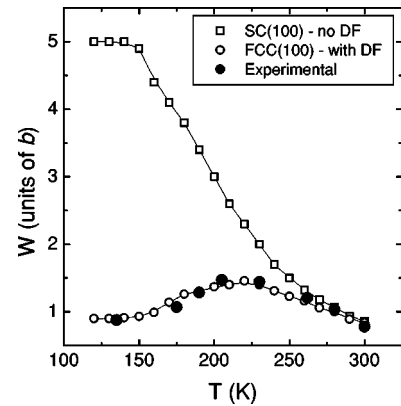


FIG. 23. W_d vs. T for 25 ML Ag/Ag(100) films deposited with $F \approx 0.02 \text{ ML/s}$ from experiments (closed circles), the FCC “square island” model (open circles), and the SC “square island” model (open squares).

and [110] close-packed step edges. Figure 23 shows a snapshot of the predicted morphology of a 25 ML film grown at 230 K. For comparison, we also show W_d behavior for this model with the same parameters as above, but for a SC geometry (on-top adsorption sites and no downward funneling). The comparison demonstrates that DF in the model with an fcc(100) geometry produces the decrease in W_d below 200 K.

Next, we discuss the predictions of the “square island” model for characteristic lateral lengths (focusing on D_{av}) in

25 ML films. One finds that for $T=175$, 205, and 230 K, the model predictions of $D_{av}=2.3$, 5.6, and 6.6 nm (in the [110] direction), respectively, are much smaller than the experimental values of 7.7, 11.9, and 13.1 nm, respectively. Apparently, the lack of restructuring of island pairs after collision in the model artificially inhibits the development (i.e., the increase) of the lateral correlation lengths. This lack of restructuring may also enhance agreement with experimental W_d for T below 200 K, which seems artificially good given the poor description of the lateral lengths.

*Current address: Department of Chemical Engineering, University of California, Berkeley, CA 94720.

¹A. L. Barabasi and H. E. Stanley, *Fractal Concepts in Surface Growth* (Cambridge, New York, 1995).

²J. Villain, *J. Phys. I* **1**, 19 (1991).

³G. Ehrlich and F. G. Hudda, *J. Chem. Phys.* **44**, 1039 (1966); R. L. Schwoebel and E. J. Shipsey, *J. Appl. Phys.* **37**, 3682 (1966).

⁴*Morphological Organization in Epitaxial Growth and Removal*, edited by Z. Zhang and M. G. Lagally (World Scientific, Singapore, 1998).

⁵M. Siegert, *Phys. Rev. Lett.* **81**, 5481 (1998); J. G. Amar, *Phys. Rev. B* **60**, R11 317 (1999); L.-H. Tang, P. Smilauer, and D. D. Vvedensky, *Eur. Phys. J. B* **2**, 409 (1998).

⁶H.-J. Ernst, F. Fabre, R. Folkerts, and J. Lapujoulade, *Phys. Rev. Lett.* **72**, 112 (1994); L. C. Jorritsma, M. Bijnagte, G. Rosenfeld, and B. Poelsema, *ibid.* **78**, 911 (1997); J.-K. Zuo and J. F. Wendelken, *ibid.* **78**, 2791 (1997).

⁷J. A. Strosio, D. T. Pierce, M. Stiles, A. Zangwill, and L. M. Sander, *Phys. Rev. Lett.* **75**, 4246 (1995); K. Thürmer, R. Koch, M. Weber, and K. H. Rieder, *ibid.* **75**, 1767 (1995).

⁸W. C. Elliott, P. F. Miceli, T. Tse, and P. W. Stephens, *Phys. Rev. B* **54**, 17 938 (1996).

⁹C. R. Stoldt, K. J. Caspersen, M. C. Bartelt, C. J. Jenks, J. W. Evans, and P. A. Thiel, *Phys. Rev. Lett.* **85**, 800 (2000); in *Recent Developments in Oxide and Metal Epitaxy: Theory and Experiment*, edited by M. Yeadon, S. Chang, R. F. C. Farrow, J. W. Evans, and O. Auciello, MRS Proceedings, Vol. 619 (MRS, Pittsburgh, 2000).

¹⁰G. Constantini, F. Buatier de Mongeot, C. Boragno, and U. Valbusa, *Surf. Sci.* **459**, L487 (2000).

¹¹Special issue on *Magnetism on a Microscopic Scale* [MRS Bull. **20**, No. 10 (1995)]; K. L. Ekinici and J. M. Valles, *Phys. Rev. B* **58**, 7347 (1998).

¹²M. C. Bartelt and J. W. Evans, *Phys. Rev. Lett.* **75**, 4250 (1995); in *Evolution of Epitaxial Structure and Morphology*, edited by A. Zangwill, D. Jesson, D. Chambliss, and R. Clarke, MRS Proceedings, Vol. 399 (MRS, Pittsburgh, 1996), p. 89.

¹³J. G. Amar and F. Family, *Phys. Rev. B* **54**, 14 071 (1996); **54**, 14 742 (1996).

¹⁴J. Jacobsen, K. W. Jacobsen, P. Stoltze, and J. K. Nørskov, *Phys. Rev. Lett.* **74**, 2295 (1995).

¹⁵For a growing fcc(100) epitaxial film, where atoms sit in fourfold hollow adsorption sites, “surface atoms” can be partially covered by $k=0-4$ neighboring atoms in the layer above. Thus, in our definition of the population, Φ_j , of surface atoms, we assign a corresponding weight, $w_k=(4-k)/4$, to each atom reflecting the degree to which it is uncovered. For these w_k , one can show

that $\Phi_j = \theta_j - \theta_{j-1}$, where θ_j is the coverage of layer j . See the Appendix of J. W. Evans, *Phys. Rev. B* **39**, 5655 (1989). For the analysis of height-height correlation functions, $H(r)$, in an fcc(100) geometry, the same weighting is naturally applied. We note that behavior is not as simple as described in the text for the continuous representation: $H(r)$ for large r in the direction of [110] step edges tends to oscillate between two values both close to $2W^2$. See Ref. 32 for details.

¹⁶J. Krim, I. Heyvaert, C. Van Haesendonck, and Y. Bruynseraede, *Phys. Rev. Lett.* **70**, 57 (1993).

¹⁷Principle curvatures come from diagonalizing the 2×2 matrix with (i,j) entries $\partial^2 S / \partial x_i \partial x_j$.

¹⁸J. E. Van Nostrand, S. Jay Chey, M.-A. Hasan, D. G. Cahill, and J. E. Greene, *Phys. Rev. Lett.* **74**, 1127 (1995); see also Strosio *et al.* in Ref. 7.

¹⁹See Strosio *et al.* in Ref. 7; Zuo and Wendelken in Ref. 6.

²⁰M. Kalff, P. Smilauer, G. Comsa, and T. Michely, *Surf. Sci.* **426**, L447 (1999).

²¹P. A. Thiel and J. W. Evans, *J. Phys. Chem. B* **104**, 1663 (2000).

²²C.-M. Zhang, M. C. Bartelt, J.-M. Wen, C. J. Jenks, J. W. Evans, and P. A. Thiel, *Surf. Sci.* **406**, 178 (1998).

²³J. A. Venables, *Philos. Mag.* **27**, 697 (1973); S. Stoyanov and K. Kashchiev, *Curr. Top. Mater. Sci.* **7**, 69 (1981).

²⁴M. C. Bartelt and J. W. Evans, *Surf. Sci.* **298**, 421 (1993).

²⁵J. G. Amar and F. Family, *Phys. Rev. Lett.* **77**, 4584 (1996).

²⁶M. V. Ramana Murty and B. H. Cooper, *Phys. Rev. Lett.* **83**, 352 (1999); O. Pierre-Louis, M. R. D’Orsogna, and T. L. Einstein, *ibid.* **82**, 3661 (1999).

²⁷J. W. Evans, D. E. Sanders, P. A. Thiel, and A. E. DePristo, *Phys. Rev. B* **41**, 5410 (1990).

²⁸M. C. Bartelt and J. W. Evans, *Surf. Sci.* **423**, 189 (1999).

²⁹D. E. Sanders and J. W. Evans, in *The Structure of Surfaces III*, edited by S. Y. Tong, M. A. Hove, K. Takayanagi, and X. D. Xie (Springer-Verlag, Heidelberg, 1991) p. 38; D. M. Halstead and A. E. DePristo, *Surf. Sci.* **286**, 275 (1993).

³⁰C. L. Kelchner and A. E. DePristo, *Surf. Sci.* **393**, 72 (1997).

³¹K. J. Caspersen, C. R. Stoldt, P. A. Thiel, and J. W. Evans, in *Recent Developments in Oxide and Metal Epitaxy: Theory and Experiment*, edited by M. Yeadon, S. Chang, R. F. C. Farrow, J. W. Evans, and O. Auciello, MRS Proceedings, Vol. 619 (MRS, Pittsburgh, 2000).

³²K. J. Caspersen and J. W. Evans, *Phys. Rev. B* (to be submitted).

³³W. C. Elliott, P. F. Miceli, and P. W. Stephens, *Bull. APS* **44**, 1604 (1999).

³⁴Once an adatom hops over the edge, DF dynamics used to select lower adsorption site for the diffusing adatom. This is correct for monatomic steps. However, one should strictly incorporate the

- appropriate interlayer thermal diffusion for multiple steps, which could lead to an adatom climbing back on top of the step (Refs. 31 and 32). However, we believe that this scenario is rare, and DF dynamics suffices in the T -range of interest. For example, there is an additional barrier of about 0.1 eV (over the facet diffusion barrier of 0.1 eV) for an adatom to climb from the sides to the top of a truncated pyramid with $\{111\}$ facets as sides (Refs. 31 and 32).
- ³⁵J. Merikoski, I. Vattulainen, J. Heinonen, and T. Ala-Nissila, *Surf. Sci.* **387**, 167 (1997).
- ³⁶U. Kurpick and T. S. Rahman, *Phys. Rev. B* **57**, 2482 (1998).
- ³⁷C. Teichert, C. Ammer, and M. Klaua, *Phys. Status Solidi A* **146**, 223 (1994).
- ³⁸A. R. Layson, C. R. Stoldt, K. J. Caspersen, M. C. Bartelt, J. W. Evans, and P. A. Thiel, *Bull. APS* **45**, 203 (2000).
- ³⁹B. D. Yu and M. Scheffler, *Phys. Rev. Lett.* **77**, 1095 (1996); *Phys. Rev. B* **55**, 13 916 (1997).
- ⁴⁰M. C. Bartelt and J. W. Evans, *Surf. Sci.* **314**, L829 (1994).
- ⁴¹J. Zhong, T. Zhang, Z. Zhang, and M. G. Lagally, *Bull. APS* **45**, 506 (2000).
- ⁴²A. Bogicevic, J. Strömquist, and B. I. Lundqvist, *Phys. Rev. Lett.* **81**, 637 (1998).
- ⁴³A. F. Voter, *Proc. SPIE* **821**, 214 (1987); H. Mehl, O. Biham, I. Furman, and M. Karmi, *Phys. Rev. B* **60**, 2106 (1999); M. Breenman, G. T. Barkema, and D. O. Boerma, *Surf. Sci.* **303**, 25 (1993).
- ⁴⁴C. R. Stoldt, A. M. Cadilhe, C. J. Jenks, J.-M. Wen, J. W. Evans, and P. A. Thiel, *Phys. Rev. Lett.* **81**, 2950 (1998); A. M. Cadilhe, C. R. Stoldt, C. J. Jenks, P. A. Thiel, and J. W. Evans, *Phys. Rev. B* **61**, 4910 (2000).
- ⁴⁵In the modeling of Ref. 44, the prefactor for kink rounding was set to $\nu_e/2$ (versus ν_e for hopping along straight $[110]$ edges). However, an adatom impinging on an island edge (that cannot reach a kink site without corner rounding) can typically avoid nucleating a new layer by rounding one of two kinks. This compensates for the factor of 1/2 in the prefactor (thus justifying the expression for h_{kr} in the text).
- ⁴⁶G. Constantini, S. Rusponi, R. Gianotti, C. Boragno, and U. Valbusa, *Surf. Sci.* **416**, 245 (1998) found a nonmonotonic dependence of roughness on temperature between 100 and 500 K for sputtering of the Ag(100) surface, somewhat analogous to behavior observed during growth between 135 and 300 K.
- ⁴⁷K. R. Roos and M. C. Tringides, *Phys. Rev. Lett.* **85**, 1480 (2000).